Integrated Buried Heaters for Efficient Spectral Control of Air-Clad Microresonator Frequency Combs

Grégory Moille,[1, 2, a)] Daron Westly,[2] Edgar F. Perez,[1, 2] Meredith Metzler,[3] Gregory Simelgor,[2] and Kartik Srinivasan[1, 2]

[1)] *Joint Quantum Institute, NIST/University of Maryland, College Park, USA*

[2)] *Microsystems and Nanotechnology Division, National Institute of Standards and Technology, Gaithersburg, USA*

[3)] *Center for Nanoscale Science and Technology, National Institute of Standards and Technology, Gaithersburg, USA*

Integrated heaters are essential in the photonics toolbox, particularly for microresonator frequency tuning through the thermo-refractive effect. Resonators that are fully embedded in a solid cladding (typically SiO_2) allow for straightforward lossless integration of heater elements. However, air-clad resonators, which are of great interest for short wavelength dispersion engineering and direct interfacing with atomic/molecular systems, do not usually have similarly low loss and efficient heater integration through standard fabrication. Here, we develop a new approach in which the integrated heater is embedded in SiO_2 below the waveguiding layer, enabling more efficient heating and more arbitrary routing of the heater traces than possible in a lateral configuration. We incorporate these buried heaters within a stoichiometric Si_3N_4 process flow that includes high-temperature (>1000 °C) annealing. Microring resonators with a 1 THz free spectral range and quality factors near 10^6 are demonstrated, and the resonant modes are tuned by nearly 1.5 THz, a 5× improvement compared to equivalent devices with lateral heaters. Finally, we demonstrate broadband dissipative Kerr soliton generation in this platform and show how the heaters can be utilized to aid in bringing relevant lock frequencies within a detectable range.

Since their discovery, frequency combs have yielded a plethora of applications – spectroscopy[1], optical clocks[2], frequency synthesis[3], and distance ranging[4]. Their integration on chip through the use of dissipative Kerr soliton (DKS) states in different platforms[5–10] has led to a focus on low power[11] and low footprint[12] devices for deployable metrology outside of the laboratory[13]. The realization of octave-spanning microcombs has been made possible by harnessing unprecedented control of integrated microresonator dispersion[13], and the additional ability to overlap their spectra with relevant atomic optical transition frequencies[14] has helped spur interest in their use in portable optical atomic clocks[2,15]. In such applications, the frequency comb acts as a gear box[13] translating the optical frequency stability of a comb tooth locked to an atomic transition to a microwave frequency through the DKS repetition rate [Fig. 1(a)]. However, the comb needs to be fully stabilized when realizing such a frequency division scheme. In the clock case, the carrier-envelope offset f_{ceo} (i.e. the shift from the zero frequency) [Fig. 1(b)] needs to be locked along with a comb tooth close enough to the optical atomic transition frequency, here called f_{lock} [Fig. 1(c)]. Their locking makes the system in Fig. 1(a) stiff, in the sense that only a single set of geometric parameters (ring width and thickness combination) will provide for enough power enhancement at the frequencies of interest (often at the location of dispersive waves (DWs)) while bringing a comb tooth sufficiently close to the atomic transition frequency. Yet,

each of these goals is essentially driven by two different parameters: the DW spectral position is defined by the cavity dispersion while f_{lock} (the beat-note between a comb tooth and the optical atomic transition) and f_{ceo} can be controlled by a simple uniform spectral shift of the comb. Therefore, integrated heaters appear as a suitable solution, leveraging spectral tuning via the thermo-refractive effect[16] and compatibility with $\chi^{(3)}$ microcomb platforms. Frequency tuning ranging up to hundreds of gigahertz has been demonstrated[17–20], though mostly in resonators fully embedded in a silica cladding.

The use of air-clad devices is, however, often desirable for dispersion engineering. Indeed, as silica presents increasingly normal dispersion as wavelengths become shorter, it is easier to compensate for the normal dispersion of Si_3N_4 through geometry in absence of a material cladding. This has been demonstrated in different contexts in microresonator nonlinear optics, including optical parametric oscillators reaching visible wavelengths[22] and microcombs whose spectral extent reaches atomic transition frequencies in the short near-infrared and near-visible[21]. In addition, an air top cladding presents the advantage of allowing post-fabrication processing to tune the geometrical dispersion if needed[23]. Direct integration of the heater to the side of the ring results in poor heat build-up at the ring core [Fig. 1(d.i)], caused by the air trenches that act as an insulator but are essential to create the ring during the lithography and etch fabrication steps. The alternative approach we propose in this paper is to bury the integrated heater below the ring resonator [Fig. 1(d,ii)], where a few micrometer gap of silica separates the metal from the optical layer, resulting in no
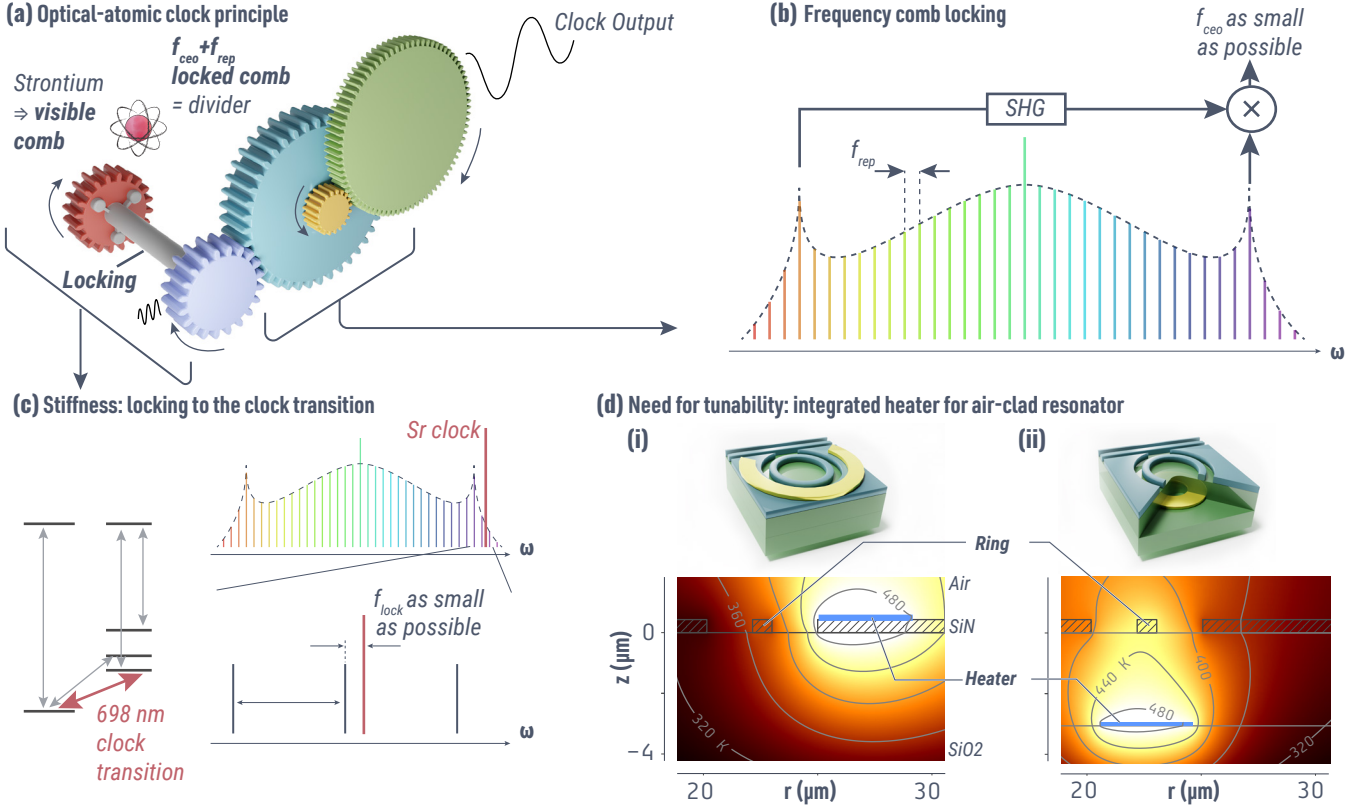
[a)]Electronic mail: gmoille@umd.edu

Fig. 1 – **Tuning and control of the DKS microcomb with the buried heater** — **(a)** Concept of an optical frequency comb acting as a frequency divider, depicted as a gearbox and inspired by Ref. 13, where the stability of a comb tooth in the optical domain is divided down to the microwave domain with the clock output being the microcomb repetition rate. For the division to be as low noise as possible, the frequency comb needs to be locked. This means that the carrier-envelope offset (f_{ceo}) and a single comb tooth frequency need to be locked. **(b)** Concept of f_{ceo} detection and locking. A tooth from an octave-spanning frequency comb and the second harmonic of a low-frequency tooth from the same comb are interfered with each other to retrieve f_{ceo}, which can, in principle, range from 0 to $f_{rep}/2$ and thus potentially be outside the photodetector bandwidth when f_{rep} is large (typical for microcombs). The octave span of the microcomb is obtained thanks to dispersive waves (DWs), where the cavity dispersion allows for comb tooth resonance enhancement at the targeted frequencies. **(c)** The clock relies on the locking of one comb tooth to the optical transition of an atomic reference, for instance, ^{87}Sr at 698 nm. Therefore, one comb tooth must be close enough to this optical transition to be locked. **(d)** As dispersion mostly impacts the position of a comb tooth that is amplified through DW enhancement, a control knob to shift the whole frequency comb is needed. Integrated heaters that leverage the thermo-refractive effect can provide this functionality. However, an air-clad ring is needed to support the dispersion required to reach the 698 nm wavelength of the ^{87}Sr reference[21]. Ergo, two possibilities exist: lateral heating (i) and the new buried heater technology introduced here (ii). Finite element method simulations show that the heat build-up is much more efficient in the case of the buried heater, with the temperature inside the ring reaching 420 K against only 365 K for the same heating power.

change in the ring losses. Due to the continuous path for heat transfer between the heater and ring layers, the efficiency of such a buried heater is much higher than for the lateral one, confirmed by thermal simulation [Fig. 1(d)]. We demonstrate the fabrication of such unique integrated heaters, which are wire-bonding ready, for integration in optical clock systems. In addition, fully embedding the heater in silica and subsequently planarizing the silica layer makes the remainder of the fabrication process compatible with a typical Si photonics process flow[24]. We experimentally show the high tuning efficiency of the system, where a resonator mode shift of 1.5 THz (equal to $1.5\times$ the resonator free spectral range (FSR)) is achieved without degradation of the resonator quality factor and with limited cross-talk. While tuning of air-clad resonators has numerous potential applications, including in sensing and coupling to gas-phase quantum emitters such as neutral alkali atoms, we showcase the utility of

these heaters in the context of broadband DKS microcombs. We experimentally demonstrate the tunability of the microcomb with an estimated shift of f_{ceo} of 15 % of the FSR and an estimated shift of the locked optical clock frequency f_{lock} over a range of close to 2 FSR. At the same time, little modification to dispersion – and hence the DW position – occurs.

The fabrication of the system [Fig. 2(a)] starts with a standard commercial silicon substrate with a 3 μm thick thermal oxide. We then define the heater pattern using a direct-write lithography maskless aligner (MLA)[25] [Fig. 2(a-i)]. The platinum is then deposited (electron beam evaporation) and lifted off. Another layer of 2.8 μm of SiO_2 is deposited above the heater layer using a 180 °C low-temperature high-density plasma chemical vapor deposition (HDPCVD) process [Fig. 2(a-ii)]. We anneal the wafer at 1000 °C for three hours to allow for the best material and the lowest absorption. Thanks to the low dif-
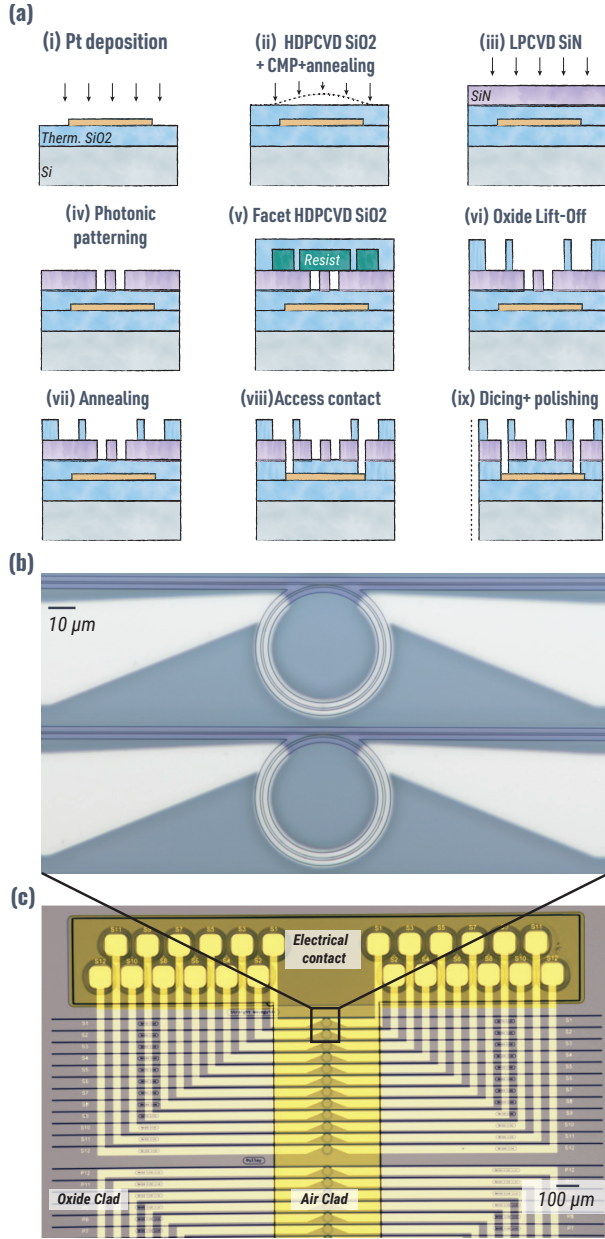
Fig. 2 – **Buried heater fabrication** – **(a)** Process flow starting with a commercial silicon wafer with thermal silicon dioxide (SiO_2). (i) Deposition of the platinum heater layer, lifted-off from previously patterned resist. (ii) Burying the heater in another layer of (HDPCVD) SiO_2. This layer needs to be planarized through CMP because of the metal underneath. An annealing step at 1000 °C for 3 hours is then performed. (iii) Resumption of the standard fabrication process with 430 nm Si_3N_4 film deposition through LPCVD followed by (iv) e-beam patterning and RIE etching to create the photonics layer. (v-vii) Oxide lift-off using low-temperature HDPCVD for air-clad rings with oxide-clad facets, followed by annealing. (viii) A last etch step through Si_3N_4 and SiO_2 to enable electrical access to the heater layer. (ix) Dicing and polishing of the chip for testing. **(b)** Optical image of the buried heater to demonstrate the alignment of the metal layer with the photonics one. **(c)** Optical image of the chip, showing how the buried heater fabrication enables arbitrary routing of the metal layer with respect to the waveguide layer.

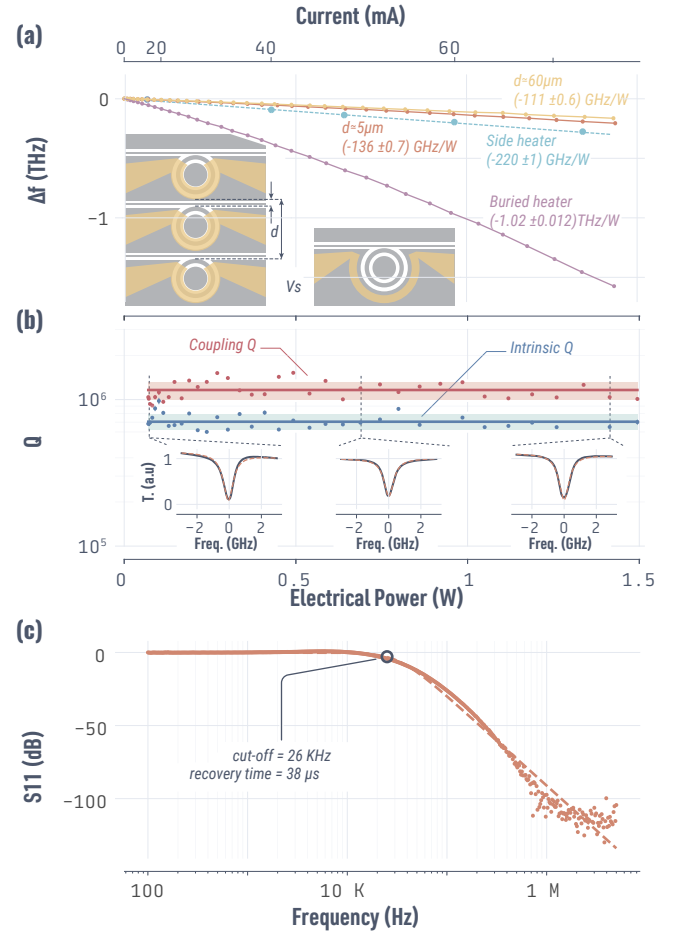fusivity of metal into silica[26], the buried heater remains

Fig. 3 – **Linear characterization of the buried heater resonator system** – **(a)** Resonant frequency shift probed around 309 THz (970 nm) for the buried heater compared to the lateral heater for the same nominal resonator-waveguide system. Cross-talk is characterized by measuring the frequency shift of neighboring rings, resulting in a cross-talk of $\Xi \approx 13$ % for a neighboring device separated by 5 μm from the target device. Devices with a larger separation show only a weak reduction in Ξ. **(b)** Intrinsic (Q_0, blue) and coupling (Q_c, red) quality factor for different electrical power, *i.e.* temperature. The absence of variation in Q_c shows that no noticeable thermal expansion happens in the system, and the geometry remains unchanged. The error bars are within the marker size. The three insets are representative transmission spectra at different power (temperature). **(c)** Frequency response of the buried heater under small-signal modulation, using a vector network analyzer to apply the modulation and coherently photodetect the transmitted signal. The value of ≈ 38 µs obtained at the 3 dB cut-off is consistent with the typical bandwidths of state-of-the-art thermal frequency shifters.

geometrically intact, and the silica layer exhibits low absorption after the annealing. A chemical-mechanical polishing (CMP) step [Fig. 2(a-ii)] is done to create a flat surface before low-pressure chemical vapor deposition (LPCVD) of a 430 nm thick film of silicon nitride[27] [Fig. 2(a-iii)]. From this point on, the process is the same as our regular nano-patterning and fabrication of air-clad ring resonators[23]. The ring resonator patterns are created through electron-beam lithography, with the patterns aligned to the underlying buried heaters us-

ing metal alignment marks that are created within the heater layer. The electron-beam resist is used as a mask for a CHF$_3$ reactive ion etch (RIE) of the silicon nitride [Fig. 2(a-iv)]. In order to maintain an air-clad ring resonator for dispersion purposes while allowing for low insertion losses, a lift-off of low-temperature HDPCVD SiO$_2$ using nLOF resist is performed [Fig. 2(a-v,vi)] as described in ref. 23. The last annealing step is performed to anneal the silicon nitride film, which has been shown to reduce absorption in the C-band through reducing N-H bonds[28] [Fig. 2(a-vii)]. Finally, an inductively coupled plasma (ICP) etch through the silicon nitride and the substrate silica, combined with a one minute 6:1 buffered oxide etch dip, reveals the metal layer for electrical contact [Fig. 2(a-viii)]. The chip is then diced and polished for optical testing [Fig. 2(a-ix)].

We proceed to characterize the linear performance – spectral tuning, cross talk, and speed – of the buried integrated heater. The experimental setup consists of a continuously tunable laser (CTL) around 1060 nm, probing a single resonant mode of the cavity. The chip is placed on an aluminum sample holder not thermally connected to the optical table (see supplementary material). Heaters are addressed from the electrical pads with DC probes connected to a current source producing up to 1.5 W of electrical power. We measure the electrical resistance of the integrated heater to be $R \approx 260$ Ω, of the same order of magnitude as typical integrated heaters[17,18]. Injecting 1.2 W of electrical power (*i.e.* a current of 67 mA), we measure a frequency shift of the resonance of more than 1.5 THz, corresponding to an ≈ 1.5 FSR red-shift [Fig. 3(a)]; amongst other things, this guarantees the ability to tune one of the microresonator's modes onto resonance with any fixed pump laser wavelength. From simulations (see supplementary material), this frequency shift is consistent with an increase in temperature at the ring above 900 K. We note that this frequency shift is quite large compared to state-of-the-art integrated heaters in the silicon nitride nonlinear photonics platform that can be obtained through foundry fabrication[29], where a shift of only 1/2 of an FSR was achieved for the same electrical power. The efficiency of the buried heater is $\eta_0 = (-1.02 \pm 0.012)$ THz/W, an improvement by a factor 5 compared to the lateral heater efficiency of $\eta_{\text{side}} = (-220 \pm 1)$ GHz/W. The uncertainty estimation arises from the standard deviation in the confidence interval for the linear fit of the frequency shift with electrical power. In addition, the cross-talk of the integrated heater is limited. The next ring resonator, with its closest point from the neighboring active heater of about 5 µm – a relatively tight separation considering the waveguide access needed to address the resonator optically – only shows a thermal shift of $\eta_{+1} = (-136 \pm 0.7)$ GHz/W. Therefore, the cross-talk of our system can be defined by $\Xi = \eta_{+1}/\eta_0 \approx 13$ %. Interestingly, the cross-talk is not highly dependent on the distance from the heater. Indeed, the second neighbor from the active heater shows a spectral shift of $\eta_{+2} = (-111 \pm 0.6)$ GHz/W, showing

that a significant portion of the chip is heating. Therefore, cross-talk could be further improved through an appropriate thermal shunt through the backside of the chip.

We proceed to consider the impact of the buried heater on the optical quality factor of the ring resonator [Fig. 3(b)]. We found that the intrinsic quality factor, in addition to being similar to that of our regular fabrication without the metal layer of $Q_0 \approx 0.75 \times 10^6$ (Ref. 23), remains unchanged for any temperature and electrical power applied to the system. Moreover, we measure that the coupling quality factor $Q_c \approx 1 \times 10^6$ stays fixed at any temperature, highlighting the little thermal expansion of the system, resulting in a fixed geometry with temperature. Our coupling is based on a straight waveguide, but in the future, using a pulley-like coupling, which is more sensitive to geometrical variations[30], would give a better estimate of the extent to which the thermal expansion is negligible. We also performed dynamical measurements in the small signal regime using a vector network analyzer to measure the recovery time of the buried heater and the frequency up to which the system can function [Fig. 3(c)]. It exhibits a 3 dB cut-off at about 26 kHz, which corresponds to a recovery time of the system of $\approx$38 µs. It is worth noting that this value is similar to that of integrated heaters on top of silica-clad rings[17], and is essentially limited by the thermal lifetimes of silicon nitride and silica[8]. We note that the SiO$_2$ gap between the microring and the heater has not been optimized and remains large (2.8 µm). Further engineering of this distance could help increase the thermal recovery speed and even increase the heater efficiency for static frequency tuning. In addition, reduction of thermal cross-talk and improved heater efficiency may also be realized through trench isolation of the heaters, for example, during or after step viii of the fabrication process.

The integrated buried heater presented here shows a high efficiency with a large thermo-refractive mediated spectral shift of the resonant mode. It remains to characterize how the thermal tuning of a ring resonator impacts the metrics associated with the optical atomic clock frequency comb, namely f_{rep}, f_{ceo} and f_{lock}. In previous work, it has been demonstrated that thermal tuning of the ring resonator allows for small tuning of f_{rep}[17]. Here, we also proceed to characterize other metrics to assess the impact of the thermal tuning on the cavity dispersion, f_{ceo}, and f_{lock}, representing three other important quantities for efficient microcomb application in optical atomic clocks. To do so, we create dissipative Kerr soliton microcombs at different electrical powers [Fig. 4(a)]. Interestingly, the overall shape of the frequency comb remains mostly the same, with only a slight shift of the DW position, despite introducing another dispersion contribution. Indeed, the variation of the effective refractive index with temperature is wavelength-dependent given the discrepancy in the thermo-refractive coefficient between Si$_3$N$_4$ $(\partial n/\partial T = 2.5 \times 10^{-5}$ K$^{-1})$[31,32], SiO$_2$ $(\partial n/\partial T = 1 \times 10^{-5}$ K$^{-1})$[31] and air $(\partial n/\partial T \equiv 0$ K$^{-1})$ and the variation of the effective mode area, which decreases
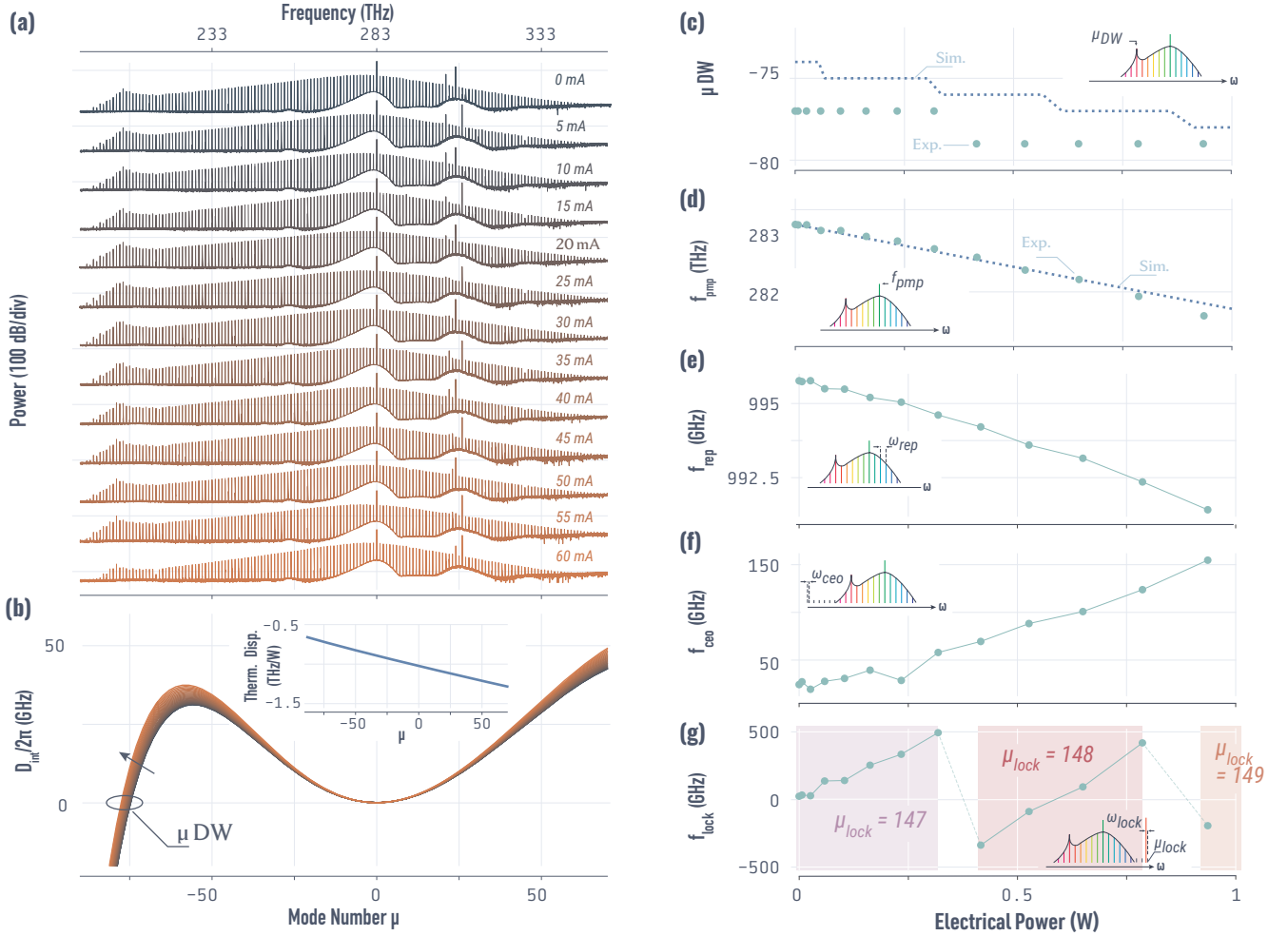
Fig. 4 – **Tuning and control of the DKS microcomb with the buried heater** — **(a)** Single DKS microcomb generated at different currents (and temperatures) through the buried heater, when pumped around 284 THz (1056 nm). The spectra is obtained through active "cooling" of the resonator using a 309 THz to 312 THz cross-polarized and counter-propagating secondary pump. The cooler frequency is changed to obtain the soliton, yet its frequency does not impact nonlinear dynamics. The DW at low frequency (long wavelength) is only slightly shifted by two comb teeth, showcasing the small, yet not negligible, dispersion of the effective (i.e., mode-weighted) thermo-refractive index. **(b)** Simulated integrated dispersion for the different current values in (a), accounting for the dispersion in the thermo-refractive index (inset) resulting from the variation in modal overlap with the Si_3N_4, SiO_2, and air regions. **(c)** Shift in the dispersive wave mode number with the increase in current (electrical power), including both the measured (circles) and simulated (dashed line) values, where the simulations are based on the integrated dispersion calculation in (b). **(d)** Frequency shift of the pump with increase in current (electrical power). **(e)** Extracted shift of the repetition rate. The repetition rate is obtained through wavemeter calibration of the pump wavelength and measuring with an optical spectral analyzer the comb tooth at $\mu = -76$. The OSA resolution is 20 pm (i.e., 2.5 GHz resolution), resulting in a measurement error of about 32 MHz (error bars are within the data point size). **(f)** Extracted f_{ceo} shift with electrical power from the extracted f_{rep} and the wavemeter calibrated f_{pmp}. **(g)** Extracted f_{lock} (blue circles) assuming a comb tooth near the ^{87}Sr transition at 698 nm. Here, we extrapolate the closest comb tooth frequency based on f_{rep} and f_{ceo} from (e) and (f). The buried heater allows for tuning of two consecutive comb teeth across the reference frequency (green circles), allowing a full tuning of f_{lock} between [-$f_{rep}/2$,$f_{rep}/2$].

with higher frequency (or mode number) [Fig. 4(b)]. The integrated dispersion, as obtained from finite element method simulations considering Joule heating, temperature distribution, and thermo-refractive coefficient (see supplementary material) show only a slight modification across the thermal tuning range. Therefore, the dispersive waves – essential for achieving octave spans and self-referencing of a microcomb – would remain mostly unchanged despite variation of the above parameters. As reported in Fig. 4(c), the experimental DW shift is only two modes, from $\mu = -77$ to $\mu = -79$, and shows a slight discrepancy from finite element method simula-

tions ($\mu = -74$ to $\mu = -78$). Although the overall shape of the DKS microcomb remains unchanged, its fundamental characteristics of relevance for clock applications – repetition rate and carrier-envelope offset frequency – are tuned with the electrical power injected. As seen previously, the resonances are red-shifted with the electrical power, ergo the pump frequency is also red-shifted [Fig. 4(d)]. As the refractive index of the material increases with the temperature, the group index should also increase, resulting in a lower repetition rate of the DKS circulating in the resonator, as measured experimentally [Fig. 4(e)]. Given the repetition rate shift and

the shift of the pump resonance, it is expected that f_{ceo} will also vary. We extract it from the measurements of f_{pmp} and f_{rep} as $f_{\text{ceo}} = f_{\text{pmp}} - N f_{\text{rep}}$, where N is the integer that brings f_{ceo} within the range $[-f_{\text{rep}}/2, +f_{\text{rep}}/2]$, and find that f_{ceo} tuning of more than 100 GHz (*i.e* about 10 % of f_{rep}) is achievable [Fig. 4(f)]. This tuning can be crucial to allow for f_{ceo} to be shifted into a detection bandwidth of a photodetector. Finally, we demonstrate the possibility of tuning f_{lock} to a stabilized optical reference [Fig. 4(g)]. Here, we have assumed a comb tooth is present near the ^{87}Sr transition at 698 nm. In practice, our demonstrated combs in this work do not extend to this wavelength due to poor comb extraction resulting from the straight waveguide coupling scheme employed[30]; however, we have demonstrated similar combs (without heaters) extending to 698 nm using optimized pulley couplers[21]. Finally, we note that because the f_{lock} comb tooth mode order is large, it provides a large multiplicative factor on the temperature-induced shift in f_{rep}. Thus, with only 1 W of electrical power, f_{lock} shifts across 3 different comb teeth, constituting a span $> 2.5 f_{\text{rep}}$.

In summary, we have demonstrated a new technique to integrate efficient micro-heaters on-chip with an air-cladding resonator, by burying the heater below the optical device layer. Once the buried heater is patterned, encased in SiO_2, and planarized, the subsequent process flow is the same as for standard Si_3N_4 photonic devices. We show that such a buried heater is $5\times$ more efficient than lateral heaters and exhibits low cross-talk, which could be even further improved by a proper thermal shunt of the chip. We then demonstrate the use of the heaters with broadband microcombs and measure/extract tuning of critical comb parameters for use in optical atomic clocks. While the microcomb measurements are indicative of the use of the buried heater technology for nonlinear integrated photonics applications, we envision many other uses in scenarios for which air cladding is required. This in particular would include microresonator-based sensors[33] and cavity QED experiments with gas-phase atoms[34,35], where both the wide tuning range and negligible impact on resonator quality factor are important factors.

Data availability
The data that supports the plots within this paper and other findings of this study are available from the corresponding authors upon reasonable request.

References

[1] A. Dutt, C. Joshi, X. Ji, J. Cardenas, Y. Okawachi, K. Luke, A. L. Gaeta, and M. Lipson, Science Advances **4**, e1701858 (2018).

[2] Z. L. Newman, V. Maurice, T. Drake, J. R. Stone, T. C. Briles, D. T. Spencer, C. Fredrick, Q. Li, D. Westly, B. R. Ilic, B. Shen, M.-G. Suh, K. Y. Yang, C. Johnson, D. M. S. Johnson, L. Hollberg, K. J. Vahala, K. Srinivasan, S. A. Diddams, J. Kitching, S. B. Papp, and M. T. Hummon, Optica **6**, 680 (2019).

[3] D. T. Spencer, T. Drake, T. C. Briles, J. Stone, L. C. Sinclair, C. Fredrick, Q. Li, D. Westly, B. R. Ilic, A. Bluestone, N. Volet, T. Komljenovic, L. Chang, S. H. Lee, D. Y. Oh, M.-G. Suh, K. Y. Yang, M. H. P. Pfeiffer, T. J. Kippenberg, E. Norberg, L. Theogarajan, K. Vahala, N. R. Newbury, K. Srinivasan, J. E. Bowers, S. A. Diddams, and S. B. Papp, Nature **557**, 81 (2018).

[4] M.-G. Suh and K. J. Vahala, Science (New York, N.Y.) **359**, 884 (2018).

[5] F. Leo, S. Coen, P. Kockaert, S.-P. Gorza, P. Emplit, and M. Haelterman, Nature Photonics **4**, 471 (2010).

[6] T. Herr, V. Brasch, J. D. Jost, C. Y. Wang, N. M. Kondratiev, M. L. Gorodetsky, and T. J. Kippenberg, Nature Photonics **8**, 145 (2014).

[7] X. Xue, Y. Xuan, Y. Liu, P.-H. Wang, S. Chen, J. Wang, D. E. Leaird, M. Qi, and A. M. Weiner, Nature Photonics **9**, 594 (2015).

[8] Q. Li, T. C. Briles, D. A. Westly, T. E. Drake, J. R. Stone, B. R. Ilic, S. A. Diddams, S. B. Papp, and K. Srinivasan, Optica **4**, 193 (2017).

[9] H. Guo, M. Karpov, E. Lucas, A. Kordts, M. H. P. Pfeiffer, V. Brasch, G. Lihachev, V. E. Lobanov, M. L. Gorodetsky, and T. J. Kippenberg, Nature Physics **13**, 94 (2017).

[10] G. Moille, L. Chang, W. Xie, A. Rao, X. Lu, M. Davanco, J. E. Bowers, and K. Srinivasan, Lasers & Photonics Reviews **14**, 2000022 (2020).

[11] B. Stern, X. Ji, Y. Okawachi, A. L. Gaeta, and M. Lipson, Nature **562**, 401 (2018).

[12] Z. Ye, F. Lei, K. Twayana, M. Girardi, P. A. Andrekson, and V. Torres-Company, Laser & Photonics Reviews **16**, 2100147 (2022).

[13] S. A. Diddams, K. Vahala, and T. Udem, Science (New York, N.Y.) **369**, eaay3676 (2020).

[14] S.-P. Yu, T. C. Briles, G. T. Moille, X. Lu, S. A. Diddams, K. Srinivasan, and S. B. Papp, Physical Review Applied **11**, 044017 (2019).

[15] T. E. Drake, T. C. Briles, J. R. Stone, D. T. Spencer, D. R. Carlson, D. D. Hickstein, Q. Li, D. Westly, K. Srinivasan, S. A. Diddams, and S. B. Papp, Physical Review X **9**, 031023 (2019).

[16] A. J. Bosman and E. E. Havinga, Physical Review **129**, 1593 (1963).

[17] X. Xue, Y. Xuan, C. Wang, P.-H. Wang, Y. Liu, B. Niu, D. E. Leaird, M. Qi, and A. M. Weiner, Optics Express **24**, 687 (2016).

[18] C. Joshi, J. K. Jang, K. Luke, X. Ji, S. A. Miller, A. Klenner, Y. Okawachi, M. Lipson, and A. L. Gaeta, Optics Letters **41**, 2565 (2016).

[19] Ó. B. Helgason, F. R. Arteaga-Sierra, Z. Ye, K. Twayana, P. A. Andrekson, M. Karlsson, J. Schröder, and Victor Torres-Company, Nature Photonics **15**, 305 (2021).

[20] A. Tikan, J. Riemensberger, K. Komagata, S. Hönl, M. Churaev, C. Skehan, H. Guo, R. N. Wang, J. Liu, P. Seidler, and T. J. Kippenberg, Nature Physics **17**, 604 (2021).

[21] G. Moille, D. Westly, G. Simlegor, and K. Srinivasan, in *CLEO: Science and Innovations* (Optica Publishing Group, 2022) pp. SW4H–6.

[22] X. Lu, X. Lu, X. Lu, G. Moille, G. Moille, A. Rao, A. Rao, D. A. Westly, K. Srinivasan, and K. Srinivasan, Optica **7**, 1417 (2020).

[23] G. Moille, D. Westly, N. G. Orji, and K. Srinivasan, Applied Physics Letters **119**, 121103 (2021).

[24] D. Thomson, A. Zilkie, J. E. Bowers, T. Komljenovic, G. T. Reed,

L. Vivien, D. Marris-Morini, E. Cassan, L. Virot, J.-M. Fédéli, J.-M. Hartmann, J. H. Schmid, D.-X. Xu, F. Boeuf, P. O'Brien, G. Z. Mashanovich, and M. Nedeljkovic, Journal of Optics **18**, 073003 (2016).

[25] Certain commercial products or names are identified to foster understanding. Such identification does not constitute recommendation or endorsement by the National Institute of Standards and Technology, nor is it intended to imply that the products or names identified are necessarily the best available for the purpose.

[26] J. D. McBrayer, R. M. Swanson, and T. W. Sigmon, Journal of The Electrochemical Society **133**, 1242 (1986).

[27] G. Moille, G. Moille, D. Westly, G. Simelgor, K. Srinivasan, and K. Srinivasan, Optics Letters **46**, 5970 (2021).

[28] H. J. Stein, P. S. Peercy, and R. J. Sokel, Thin Solid Films **101**, 291 (1983).

[29] A. Rao, G. Moille, X. Lu, D. A. Westly, D. Sacchetto, M. Geiselmann, M. Zervas, S. B. Papp, J. Bowers, and K. Srinivasan, Light: Science & Applications **10**, 109 (2021).

[30] G. Moille, Q. Li, T. C. Briles, S.-P. Yu, T. Drake, X. Lu, A. Rao, D. Westly, S. B. Papp, and K. Srinivasan, Optics Letters **44**, 4737 (2019).

[31] A. W. Elshaari, I. E. Zadeh, K. D. Jons, and V. Zwiller, IEEE Photonics Journal **8**, 1 (2016).

[32] G. Moille, X. Lu, A. Rao, Q. Li, D. A. Westly, L. Ranzani, S. B. Papp, M. Soltani, and K. Srinivasan, Physical Review Applied **12**, 034057 (2019).

[33] D. Yu, M. Humar, K. Meserve, R. C. Bailey, S. N. Chormaic, and F. Vollmer, Nature Reviews Methods Primers **1**, 83 (2021).

[34] J. L. O'Brien, A. Furusawa, and J. Vučković, Nature Photonics **3**, 687 (2009).

[35] T.-H. Chang, X. Zhou, M. Zhu, B. M. Fields, and C.-L. Hung, Applied Physics Letters **117**, 174001 (2020).
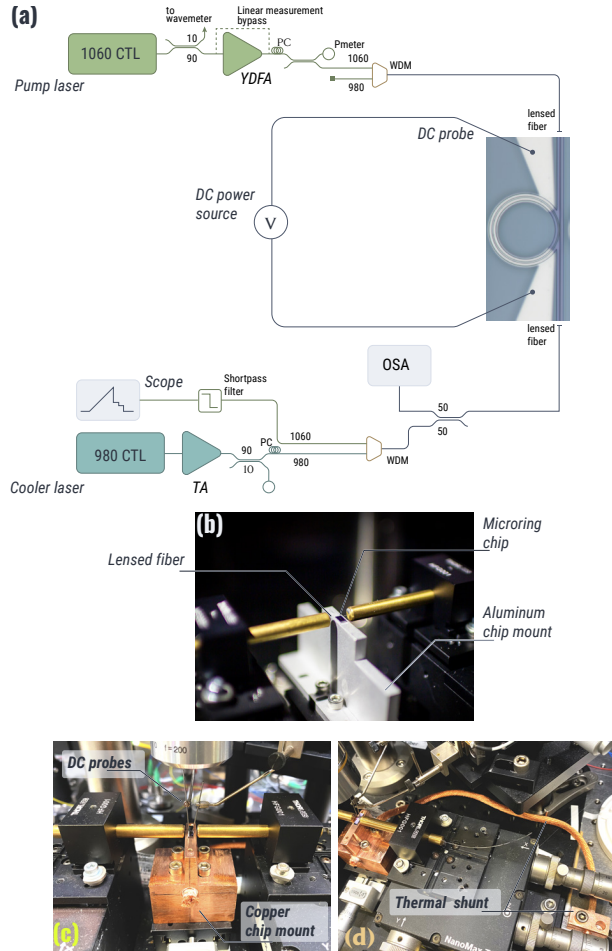
S-1. Experimental Setup

Fig. S1 – Experimental Setup: (a) Schematic of the experimental setup with a tunable laser around 1060 nm (1060 CTL) for either spectroscopy of cavity modes or to go through a YDFA amplifier for comb generation. In the latter case, an amplified 980 nm tunable laser (980 CTL) is used to actively-cool the resonator and allow for adiabatic DKS access. WDM = wavelength division multiplexer, OSA = optical spectrum analyzer, PC = polarization controller. **(b)** Close-up picture of the coupling portion of the setup with the aluminum sample holder used in Fig. 3, which acts as a thermal insulator. **(c)-(d)** Close up of the copper sample mount used in Fig. 4, which is thermally shunted to the optical table and acts as a heat sink at room temperature. This results in a much more stable coupling setup, allowing for DKS operation. Note that the coupling was stable enough that the fiber did not need to be adjusted to keep an optimal coupling for any current used in Fig. 4.

The setup used in this work is presented schematically in Fig. S1(a). The continuously tunable laser (CTL) provides tuning of the wavelength from 1010 nm to 1070 nm to perform spectroscopy, and we adjust the input light polarization such that we excite the the fundamental transverse electric (TE) modes (*i.e.*, TE_0) of the resonator, by measuring the transmission as a function of wavelength. In this *linear* case, the sample mount is made of aluminum (Fig. S1(b)), through which we no-
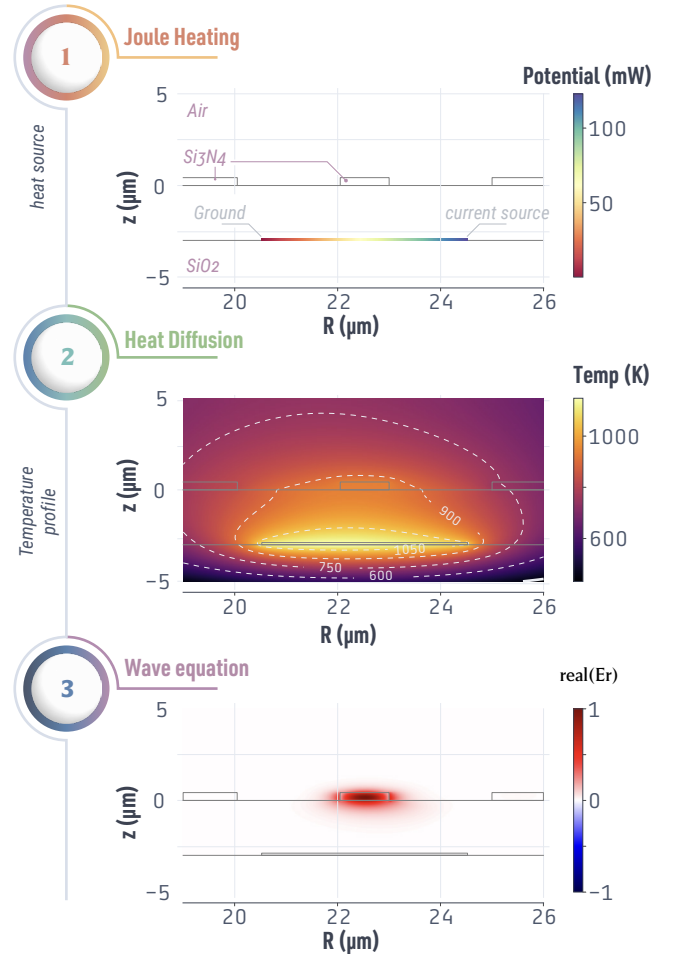

Fig. S2 – Simulation workflow to simulate spectral shifts of the resonant mode of the ring resonator: (1) we start with a Joule effect simulation in which an input current applied to the buried integrated heater results in an electrical potential and the creation of a heat source. (2) Then, we proceed to solve the Fourier heat equation to find the steady-state of the temperature profile. We apply a fixed boundary condition on the temperature at the bottom of the substrate, and an open boundary elsewhere. We map this temperature profile to the variation of the refractive index profile $\Delta T \partial n/\partial T|_{(r,z)}$. (3) This allows for the Maxwell wave equation to account for the temperature profile which will be reflected in the frequency of resonance (i.e. respecting the periodic boundary condition in ϕ, which is out of the plane of the image). We note that the figures presented are zoomed-in from the full simulation domain.

ticed experimentally a limited heat diffusion and an overall increase of the chip temperature, resulting in coupling instability for creation of DKS. In contrast, we use a copper sample mount linked to the optical table (Fig. S1(c)-(d)) to perform nonlinear measurements, where an ytterbium-doped fiber amplifier (YDFA) is used to produce adequate optical power around 1060 nm, while a (counterpropagating and orthogonally polarized) 980 nm laser is used to actively cool the resonator to reach DKS states adiabatically. The improved thermal conductivity and heat sinking to the optical table makes the impact of the buried heaters more local, and the overall chip temperature is not increased as much as in the case of the Al sample mount. Importantly, the overall

frequency tuning range achieved by the buried heater is nearly the same regardless of the mount (i.e., comparing Fig. 3(a) and Fig. 4(d)). Interestingly, we believe that use of the copper mount also helps mitigate convective air flows, making the setup much more stable. This has allowed us to measure the DKS states at different electrical powers in Fig. 4 without the need to adjust the fiber position for optical coupling.

S-2. Thermal Simulations

In order to accurately account for the integrated buried heater impact on the optical mode of the ring resonator, we performed so called *fully-coupled* simulations, where the Joule heating, heat diffusion and wave equations are solved as a coupled equations system [Fig. S2]. First, we leverage the symmetry of the system, where in a cylindrical coordinate system $\{r, \phi, z\}$, periodic boundary conditions are assumed in ϕ, simplifying the system to an effective two-dimensional one along $\{r, z\}$. The optical field is given as $E(r, \phi, z) = E(r, z)e^{im\phi}$, with m the azimuthal mode number of the ring resonance. Although the implemented heater design breaks this symmetry because it was not fully wrapped around the ring to avoid heating of the resonator-waveguide coupling region, we will assume the heat diffusion is strong enough to allow for uniform temperature in ϕ. Here, we describe the essential steps taken by the solver, although these equations are effectively solved simultaneously. We start by simulating Joule heating, where a current density is injected in the heater assuming the measured resistance of 260 Ω [Fig. S2(a)], which we use as a heat power source for the heat diffusion equation [Fig. S2(b)], allowing us to retrieve the temperature profile along $\{r, z\}$. The boundary conditions are crucial for accurate simulation, and following the improvement of the setup described in the previous section, we assume the bottom of the substrate to be at room temperature and the others as open boundaries. Simulations where the substrate thickness has been increased did not significantly change the simulations results. Although the bottom of the substrate may present a higher temperature than the one assumed here, our assumption of room temperature best reproduces the experimental data presented in Fig. 4. Finally, using a Seillmeier model to determine the refractive index of the silicon nitride and silicon dioxide layers according to ellipsometry measurements previously performed[27], and accounting for the thermo-refractive index coefficient of each material, we use the simulated profile to determine the refractive index shift $\Delta n(r, z)$ due to the heating. This allows to model the frequency shift of a given resonator mode along with complete dispersion of the resonator modes with electrical power.